



## Full length article

# Environmentally-assisted grain boundary attack as a mechanism of embrittlement in a nickel-based superalloy



A.A.N. Németh, D.J. Crudden, D.E.J. Armstrong, D.M. Collins, K. Li, A.J. Wilkinson, C.R.M. Grovenor, R.C. Reed\*

Department of Materials, University of Oxford, Parks Road, Oxford, OX1 3PJ, UK

## ARTICLE INFO

## Article history:

Received 16 November 2016

Received in revised form

15 December 2016

Accepted 16 December 2016

## Keywords:

Ni-based superalloy

Oxidation

Environmentally-assisted cracking

Ductility minima

## ABSTRACT

The loss of ductility in the high strength polycrystalline superalloy 720Li is studied in air between room temperature and 1000 °C. Tensile ductility is influenced profoundly by the environment, leading to a pronounced minimum at 750 °C. A relationship between tensile ductility and oxidation kinetics is identified. The physical factors responsible for the ductility dip are established using energy-dispersive X-ray spectroscopy, nanoscale secondary ion mass spectrometry and the analysis of electron backscatter diffraction patterns. Embrittlement results from internal intergranular oxidation along the  $\gamma$ -grain boundaries, and in particular, at incoherent interfaces of the primary  $\gamma'$  precipitates with the matrix phase. These fail under local microstresses arising from the accumulation of dislocations during slip-assisted grain boundary sliding. Above 850 °C, ductility is restored because the accumulation of dislocations at grain boundaries is no longer prevalent.

© 2017 Acta Materialia Inc. Published by Elsevier Ltd. This is an open access article under the CC BY license (<http://creativecommons.org/licenses/by/4.0/>).

## 1. Introduction

Polycrystalline  $\gamma/\gamma'$ -strengthened Ni-based superalloys are very strong, but their grain boundaries are a source of weakness at elevated temperature due to their interaction with gaseous environments containing oxygen. This problem is of particular concern when considering the application of these materials in the hot-section components needed for power generation and/or jet propulsion: these are subjected to oxidative and corrosive gas streams whilst under high stresses at temperatures in excess of 700 °C. Operating temperatures are rising markedly – due to ongoing fuel efficiency demands and the need to reduce emissions – hence damage from so-called environmentally-assisted cracking is becoming increasingly prevalent and is now the major limitation to the application of Ni-based superalloys at the higher temperatures [1]. The precise mechanism for this effect is contentious, necessitating systematic experimentation and associated characterisation at the appropriate length scale to elucidate the underlying physical and chemical factors at play.

Environmentally-assisted cracking has been proposed by some investigators to be influenced by dynamic embrittlement involving

the migration of elemental oxygen ahead of the crack front [2–5]; others propose that the phenomena is affected by stress-assisted grain boundary oxidation (SAGBO) [6–9]. The distribution of oxygen at an intergranular crack tip has been characterised recently using techniques of high spatial resolution including transmission electron microscopy combined with energy dispersive X-ray spectroscopy (EDX) [9], nanoscale secondary ion mass spectrometry (NanoSIMS) [10], and atom probe tomography [8]. These studies revealed the formation of a layered oxide structure along the  $\gamma$ -grain boundaries ahead of the cracks thus supporting a damage mechanism similar to the SAGBO concept. In general, the layering was found to be in agreement with thermodynamics: thermodynamically unstable oxides consisting of Ni, Fe and Co were found at the beginning and centre of the crack while more stable oxides consisting of Cr, Ti and Al were found closer to the interface of the oxide and metal [6,8,11]. The oxidation of secondary  $\gamma'$ -precipitates has been suggested to lead to the formation of Ni- and Al-rich oxides [8]. However, the proposed concepts so far fail to explain fully why a super-solvus heat treatment with only intragranular  $\gamma'$ -precipitates is observed to be more resistant to environmentally assisted cracking than a sub-solvus heat treatment where both intra- and intergranular  $\gamma'$ -precipitates are present [12].

In the literature, environmentally-assisted cracking is most usually recognised in the context of low-cycle fatigue and dwell-fatigue loading tests. However, the complexity of such testing

\* Corresponding author.

E-mail address: [roger.reed@eng.ox.ac.uk](mailto:roger.reed@eng.ox.ac.uk) (R.C. Reed).

combined with the substantial time and material requirements is somewhat problematic. Alternatively, Gabb et al. [13] demonstrated that inelastic failure strain of slow strain-rate tensile tests can be correlated to the dwell fatigue crack propagation rate. Here, these pioneering concepts are built upon. Sub-solvus heat treated superalloy 720Li is subjected to slow strain-rate tensile tests between room temperature and 1000 °C. Miniature test pieces of enhanced surface/volume ratio are employed, in order to accelerate the embrittlement effect and thus facilitate its study. These miniaturised tensile tests have been shown to be capable of capturing the temperature and time-dependent effects that occur during environmentally-assisted failure [14]. In the past, a temperature dependent minimum in tensile ductility [15,16] and maximum in fatigue crack propagation rate [17] was observed. This was reviewed by Woodford [18] who proposed that a mid-temperature embrittlement is not exclusively due to environmental interactions but is also linked to the grain boundary mobility. This hypothesis is not incompatible with more recent results which emphasise that the ability to reduce stresses at the crack tip by stress relaxation has an impact on an alloy's susceptibility to oxidation-assisted cracking [9,19,20].

In this study, quantitative data for the ductility of alloy 720Li are reported and the role of environmental attack is confirmed. Detailed characterisation of the crack tip processes is then carried out – notably with EDX, NanoSIMS and high resolution electron backscatter scatter diffraction (HR-EBSD) in an attempt to answer the following questions:

- (1) What is the nature of the environmentally-assisted grain boundary attack leading to intergranular crack propagation?
- (2) What is role of the deformation mechanism on the failure of the environmentally-induced damage zone?
- (3) How can we rationalise the effect of heat treatment on an alloy's susceptibility to environmentally-assisted cracking?

## 2. Experimental procedure

### 2.1. Material

In this study, the cast/wrought nickel-based superalloy alloy 720Li was used primarily. A further more limited number of tests were carried out on the powder metallurgy alloy RR1000. Nominal compositions are given in Table 1. The materials were supplied by Rolls-Royce plc. in the form of fully heat treated forgings.

Alloy 720Li has a temperature capability of around 700 °C [21]. The following sub-solvus heat treatment was applied: a solution heat treatment at 1095 °C for 4 h followed by an oil quench and a subsequent ageing heat treatment at 760 °C for 16 h. Fig. 1(a) shows the as-received microstructure of alloy 720Li prior to testing. This region was investigated using EBSD in order to calculate the  $\gamma$ -grain and primary incoherent  $\gamma'$ -precipitate size distribution, see Fig. 1(b). A Gaussian non-linear curve fit was applied in order to distinguish the average  $\gamma$ -grain size,  $d_\gamma \approx 8 \pm 3 \mu\text{m}$ , and the average intergranular primary  $\gamma'$ -precipitate size,  $d_{\gamma'} \approx 4 \pm 0.5 \mu\text{m}$ . The size of these intergranular primary  $\gamma'$ -precipitates can be determined using EBSD because their incoherency results in a crystal orientation which differs from the adjoining  $\gamma$ -grains. The measured

average  $\gamma$ -grain and primary  $\gamma'$ -precipitate size is in close agreement with previous microstructural assessment of Alloy 720Li [22–25]. The mean diameter of the intergranular secondary  $\gamma'$ -precipitates which are shown in Fig. 1(c) was found to be  $\approx 100 \text{ nm}$ . For comparison, a super-solvus heat treatment at 1170 °C was applied to alloy 720Li. Unfortunately, due to the lack of grain boundary pinning after the dissolution of the primary  $\gamma'$ -precipitates abnormal grain growth occurred; the reason can be traced to the low content of grain boundary elements (Table 1). In addition, upon cooling at requisite rates, quench cracking was observed. As a result, alloy RR1000 processed by powder metallurgy was studied additionally in both sub- and super-solvus heat treated condition. The sub-solvus heat treatment consisted of a solution heat treatment at 1120 °C for 4 h followed by an air quench and an ageing heat treatment at 760 °C for 16 h which is reported to result in a  $\gamma$ -grain size of  $d_\gamma \approx 7 \pm 2 \mu\text{m}$  and a primary  $\gamma'$ -precipitate size of  $d_{\gamma'} \approx 5 \mu\text{m}$  [26]. The super-solvus heat treatment consisted of a solution heat treatment at 1170 °C for 1 h followed by an fan air cool and an ageing heat treatment at 760 °C for 16 h. This super-solvus heat treatment was shown to increase the  $\gamma$ -grain size to  $d_\gamma \approx 30 \pm 5 \mu\text{m}$  [26]. A full characterisation of the as-received microstructure of RR1000 can be found elsewhere [9,26–28].

### 2.2. Assessment of the tensile ductility

Tensile testing was conducted between room-temperature and 1000 °C on a 5 kN Instron electro-thermal mechanical testing (ETMT) machine [29]. Miniaturised specimens of cross-section  $1 \times 1 \text{ mm}^2$  and a gauge length of 14 mm were used; the full sample length was 40 mm. The specimens were produced using wire-based electrical discharge machining (EDM), with surfaces subsequently ground to 1200 grit finish using silicon carbide grinding paper to maintain a consistent surface finish and to remove the recast layer resulting from the EDM process. Temperature measurement during testing was achieved by spot-welding a K-type thermocouple to the central portion of the specimen gauge. A minimum of three tests were performed at each condition.

Slow strain-rate tests were performed in laboratory air with an initial slow strain-rate close to  $1 \cdot 10^{-4} \text{ s}^{-1}$ . These were conducted at room temperature, 400, 500, 600 and between 700 and 1000 °C in steps of 50 °C. Consistent with the design of the ETMT machine, specimens were heated using electrical resistance by passing a direct current through the specimen. Tests were performed at a constant extension rate using a linear variable displacement transformer (LVDT). The engineering strain was used as a measure of the ductility; engineering strain is defined as  $\epsilon = [(L_f - L_0)/L_0]$ , where the gauge length extension  $L_0 - L_f$  was monitored using digital image correlation following a thermal paint pattern in the central 5 mm of the specimen where the temperature and therefore deformation is uniform [14]; the engineering stress-strain curves produced were shown to be independent to small changes of  $L^0$  (5 mm). Further but more limited testing was carried out at 800 °C using intermediate and fast initial strain-rates – close to  $1 \cdot 10^{-3}$  and  $1 \cdot 10^{-2} \text{ s}^{-1}$  – in laboratory air. Slow strain-rate tensile testing was also conducted in argon at 800 °C.

### 2.3. Measurement of the oxide kinetics

Thermo-gravimetric analysis (TGA) was conducted on  $10 \times 10 \times 1 \text{ mm}$  test pieces between 700 and 1000 °C using a Netsch Jupiter TGA rig. Prior to isothermal exposure, specimen surfaces were ground to a 1200 grit finish using silicon carbide grinding paper. In addition, all edges were chamfered. Specimens were exposed between 700 and 1000 °C in 100 °C steps to 50 ml/min laboratory air for a short exposure time of 10 min and for a

**Table 1**  
Nominal composition of alloy 720Li and RR1000 in wt-% (Ni-base).

Alloy	Ni	Cr	Co	W	Mo	Al	Ti	Ta	C	B	Zr
720Li	bal	16.0	15.0	1.25	3.0	2.5	5.0	0.0	0.015	0.015	0.035
RR1000	bal	15.0	18.5	0.0	5.0	3.0	3.6	2.0	0.027	0.015	0.06

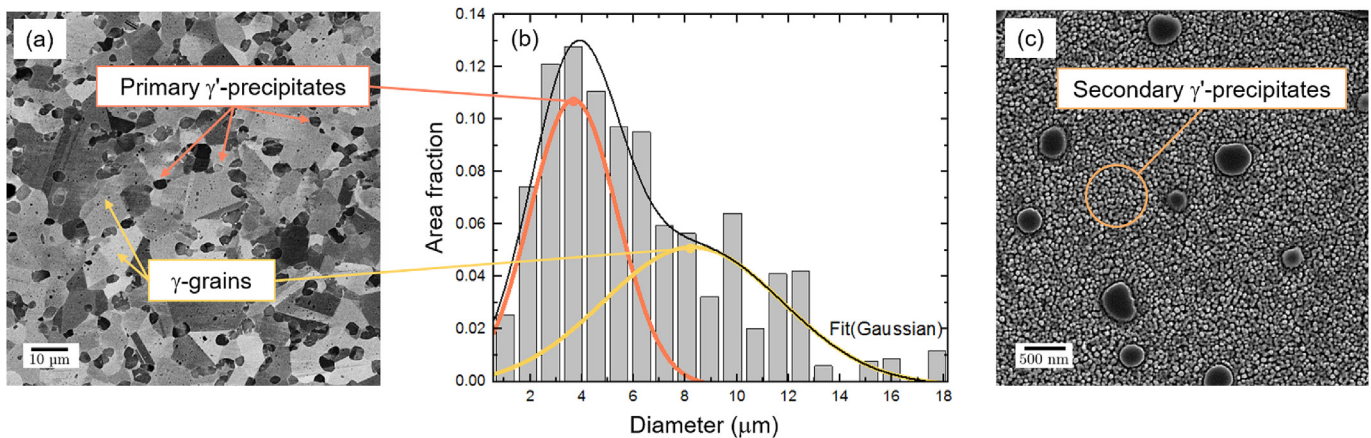


**Fig. 1.** (a) Backscattered electron image of the microstructure of alloy 720Li consisting of  $\gamma$ -grains and incoherent intergranular  $\gamma'$ -precipitates used in this study. (b) Measured size distribution using EBSD including two Gaussian type fits to determine the  $\gamma$ -grain and incoherent intergranular primary  $\gamma'$ -precipitate size distribution and the overall cumulative fit. A total number of 2443 grains were measured. (c) SEM image of a  $\gamma$ -grain after electro-chemical etching in 10% phosphoric acid showing smaller coherent intragranular primary and secondary  $\gamma'$ -precipitates.

longer exposure time of 50 h. The heating and cooling was performed in a protective argon atmosphere.

#### 2.4. Fractography and damage analysis

The microstructures both before and after testing was characterised with a JEOL 6500F FEG scanning electron microscope (SEM). Secondary/backscattered electron imaging and HR-EBSD analysis were used. Diffraction patterns were acquired with a TSL Digiview II detector - controlled with the OIM software - at the full resolution of  $1000 \times 1000$  pixels to maximise the available angular resolution, and saved for subsequent analysis. Using an in-house method to measure the lattice curvature, the distribution of geometrically necessary dislocations (GNDs) is estimated. A description of this technique is described in Wilkinson et al. [30]. Observation of the fracture surfaces following mechanical testing was carried with three dimensional (3D) optical metrology using an Alicona optical microscope. Fractography was supported by secondary electron imaging and sub-micron resolution NanoSIMS using a Cameca NanoSIMS 50 system, for details see Ref. [31]. In addition, a Zeiss Merlin FEG SEM equipped with a in column energy selective backscattered (ESB) detector and an Oxford Instruments XMax 150 mm<sup>2</sup> detector for obtaining EDX maps at a high spatial resolution was applied. Oxide scales were assessed using a Zeiss Auriga focussed ion beam (FIB) system.

### 3. Results

#### 3.1. On the temperature-dependence of the tensile ductility

Miniaturised slow strain-rate tensile tests were performed on alloy U720Li between room-temperature and 1000 °C in laboratory air. Representative engineering stress-strain curves are shown in Fig. 2(a). Three temperature regimes are seen with markedly different tensile ductility. First at low temperatures below 500 °C alloy 720Li remains ductile with a failure strain exceeding 15%. Second, a significant reduction in tensile ductility is observed at intermediate temperatures in the range 600–850 °C, with a minimum failure strain of 3% at 750 °C. Third, a high-temperature regime above 850 °C where ductility is restored. Notably, fracture was not reached at tests performed at temperatures above 900 °C. The tests were stopped at 24% due to potential necking above or below the thermocouple, which would result in an increase in

temperature in the vicinity of the reduced section (Fig. 2) as a result of the heating current [14]. The strain to failure obtained at each test temperature is summarised in Table 2. The dramatic loss in ductility in the mid-temperature regime is consistent with observations made on other superalloy systems [13,15,16,32] and can be explained as follows. At 500 °C a transition occurs between ductile transgranular and quasi-brittle intergranular failure. Therefore, intergranular crack propagation in this regime limits the tensile ductility. This is illustrated in Fig. 2(b) where tensile ductility is plotted against temperature.

The effects of both strain-rate and environment were assessed at 800 °C. The results are illustrated in Fig. 3(a) together with SEM images of cross-sections through failed specimens. At both slow and intermediate strain-rates,  $1 \cdot 10^{-4}$  and  $1 \cdot 10^{-3} \text{ s}^{-1}$  respectively, quasi-brittle failure occurred with limited strain to failure. A significant increase in elongation was noted if a fast strain-rate of  $1 \cdot 10^{-2} \text{ s}^{-1}$  was applied. Slow strain-rate tests conducted in an inert argon atmosphere at 800 °C also resulted in the tensile ductility regain. The clear effect of strain-rate and testing environment on the tensile ductility of alloy 720Li is summarised in Table 3 and suggests that the dip in ductility is indeed due to environmental interactions. Therefore, the observed environmental embrittlement is thermally-activated and dependent on the environment and the applied strain-rate.

The effect of heat treatment was assessed at 700, 750 and 800 °C. Fig. 3(b) compares the tensile ductility of sub-solvus heat treated alloy 720Li & RR1000 and super-solvus heat treated RR1000 using a slow initial strain-rate close to  $1 \cdot 10^{-4} \text{ s}^{-1}$  in laboratory air. Both sub-solvus heat treated superalloys, alloy 720Li and RR1000, failed with limited strain to failure and a minimum in tensile ductility at 750 °C, with RR1000 performing better than alloy 720Li. The same trend has been reported for fatigue crack propagation [33]. If the two variants of RR1000 are compared an significant improvement in tensile ductility due to the super-solvus heat treatment is unambiguously observed. This is in agreement with the reported decrease in dwell fatigue crack propagation rate after applying a super-solvus heat treatment to the powder metallurgy Ni-superalloy, Alloy 10 [12].

#### 3.2. On the temperature-dependence of the tensile strength

The measured 0.2% proof stress (YS) and ultimate tensile strength (UTS) of alloy 720Li is summarised in Table 2. The strength



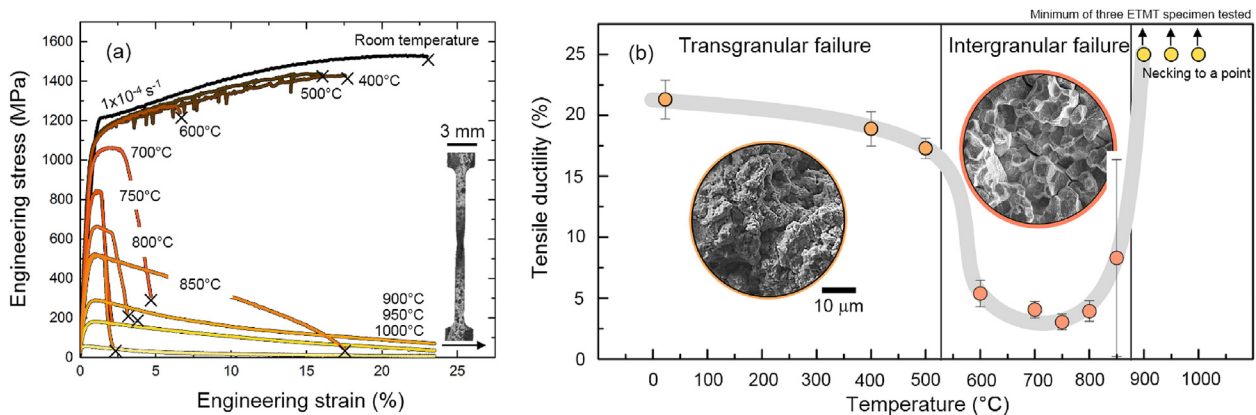


**Fig. 2.** (a) Representative stress-strain curves for alloy 720Li between room temperature and 1000 °C at an initial strain-rate close to  $1 \cdot 10^{-4} \text{ s}^{-1}$ . Between 900 and 1000 °C tests were stopped after 24% engineering strain due to the pronounced development of a neck. (b) Variation in tensile ductility with temperature for slow strain-rate tensile tests in laboratory air. Error bars represent the standard deviation of a minimum of three test repetitions. Representative types of failure below and above 500 °C are illustrated. Above 850 °C ductility is restored.

**Table 2**

Effect of test temperature on the mechanical properties of alloy 720Li when tested in laboratory air with an initial strain-rate of  $1 \cdot 10^{-4} \text{ s}^{-1}$ . Mean results and standard deviation (SD) of a minimum of three test repetitions are given.

Temperature (°C)	YS (MPa)	UTS (MPa)	Tensile ductility (%)
23	1139 ± 49	1557 ± 22	24.6 ± 1.6
400	1061 ± 21	1472 ± 36	18.9 ± 1.4
500	1051 ± 15	1447 ± 24	17.3 ± 0.9
600	1042 ± 18	1240 ± 39	5.4 ± 1.1
700	978 ± 7	1057 ± 6	4.1 ± 0.7
750	814 ± 31	863 ± 32	3.0 ± 0.7
800	601 ± 25	637 ± 23	3.9 ± 0.8
850	524 ± 31	554 ± 30	8.3 ± 8.0
900	274 ± 11	291 ± 21	>24
950	188 ± 19	202 ± 21	>24
1000	69 ± 18	71 ± 19	>24

of alloy 720Li was found to be temperature independent up to 600 °C; a result that was in good agreement to those obtained by conventional tensile tests [14]. Above 700 °C the strength is highly temperature dependent and decreases rapidly which suggests a change in the deformation mechanism. This is consistent with the

data obtained for RR1000 (Table 4). Neither YS nor UTS was affected by the testing environment, see Table 3.

The temperature dependent nature of the YS between 700 and 850 °C, where extensive environmental damage occurs, can be assessed using the following equation:

$$\sigma_y = C_1 \cdot \exp\left(\frac{Q}{RT}\right) \bigg|_{\epsilon, \dot{\epsilon}}, \quad (1)$$

where  $Q$  is an activation energy for the dominant deformation mechanism,  $R$  is the universal gas constant,  $C_1$  is a constant and  $T$  is the test temperature [34]. Applying this equation to our experimental results, a straight line was fitted to the plot of  $\ln(\sigma_y)$  versus  $1/T$  with an adjusted  $R^2$  of 97.4%. The activation energy obtained from the slope of this line was calculated to be  $Q \approx 40 \text{ kJ mol}^{-1}$ .

The YS and UTS of alloy 720Li increases with strain-rate. A difference of  $\approx 500 \text{ MPa}$  was observed between the fastest and slowest strain-rate. These findings are summarised in Table 3.

The dependence of the YS on the applied strain-rate can be expressed through:

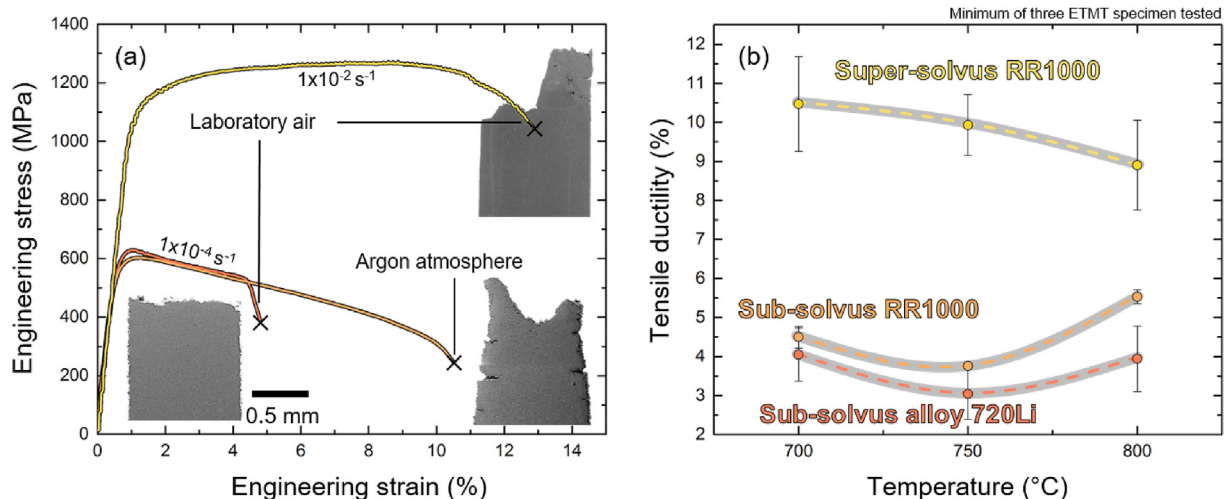


**Fig. 3.** (a) Representative stress-strain curves for alloy 720Li tested at 800 °C in laboratory air using a slow and a fast strain-rate and when tested in an argon environment. SEM images of the samples after failure demonstrate the failure mode. (b) Variation in tensile ductility between 700 and 800 °C for slow strain-rate tensile tests performed on sub-solvus alloy 720Li, sub-solvus RR1000 and super-solvus RR1000. Error bars represent the standard deviation of a minimum of three test repetitions.

**Table 3**

Effect of variations in atmosphere and initial strain-rate on the mechanical properties of Alloy 720Li when tested in laboratory air at 800 °C. Mean results and SD of a minimum of three test repetitions are given.

Atmosphere	Strain-rate (s <sup>-1</sup> )	YS (MPa)	UTS (MPa)	Tensile ductility (%)
Argon atmosphere	1 · 10 <sup>-4</sup>	596 ± 10	637 ± 22	24.6 ± 1.0
Laboratory air	1 · 10 <sup>-4</sup>	601 ± 25	637 ± 23	3.9 ± 0.8
Laboratory air	1 · 10 <sup>-3</sup>	751 ± 21	761 ± 28	2.8 ± 1.3
Laboratory air	1 · 10 <sup>-2</sup>	1102 ± 49	1298 ± 22	12.4 ± 1.0

**Table 4**

Effect of heat treatment on the YS and UTS of RR1000 when tested in laboratory air between 700 and 800 °C. Mean results and SD of a minimum of three test repetitions are given. Data for alloy 720Li is shown for comparison.

Alloy and heat treatment	Temperature (°C)	YS (MPa)	UTS (MPa)	Tensile ductility (%)
RR1000, sub-solvus	700	986 ± 12	1052 ± 6	4.5 ± 0.3
	750	823 ± 24	878 ± 25	3.8 ± 0.1
	800	624 ± 24	647 ± 20	5.5 ± 0.2
RR1000, super-solvus	700	845 ± 3	1007 ± 17	10.5 ± 1.2
	750	813 ± 3	861 ± 10	9.9 ± 0.8
	800	733 ± 12	737 ± 14	8.9 ± 1.1
720Li, sub-solvus	700	978 ± 7	1057 ± 6	4.1 ± 0.7
	750	814 ± 31	863 ± 32	3.0 ± 0.7
	800	601 ± 25	637 ± 23	3.9 ± 0.8

$$\sigma_y = C_2 \cdot (\dot{\epsilon})^m \Big|_{\epsilon, T} \quad (2)$$

where  $C_2$  is a constant and  $m$  describes the strain-rate sensitivity [35]. The strain-rate sensitivity  $m$  is the ratio of the incremental change in  $\ln \sigma$  to the resultant change in  $\ln \dot{\epsilon}$ , at a given strain and temperature. For the change in flow stress upon the rise from slow to intermediate strain-rate at 800 °C, where quasi-brittle failure is observed, a strain-rate sensitivity of  $m \approx 0.17$  was calculated. This is close to the strain-rate sensitivity determined by Gopinath et al. [24] for alloy 720Li at 750 °C for a comparable deformation rate. In addition, the activation volume ( $\Delta V$ ) can be calculated by the following equation:

$$\Delta V = \sqrt{3} kT \frac{d \ln \dot{\epsilon}}{d \sigma}, \quad (3)$$

where  $k$  is the Boltzmann constant [36]. The apparent activation volume was determined to be  $\Delta V \approx 65 b^3$  at 800 °C, where  $b = 0.26$  nm.

### 3.3. Characterisation of environmentally-assisted failure

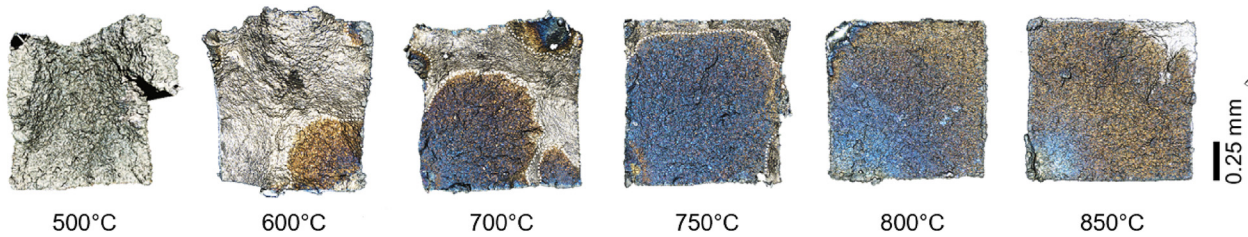
The ductility dip observed in alloy 720Li in the mid-temperature regime correlates to evidence of increased environmental damage on the fracture surfaces of the failed miniaturised tensile specimens. This increase with test temperature is illustrated in Fig. 4. Environmental damage is evident across the whole fracture surface for specimens tested above 750 °C. In general, the regions of the fracture surface that showed environmental damage failed perpendicular to the applied load in an intergranular manner, see Fig. 5. Regions without environmental damage failed at ~45° to the tensile axis; dimples and micro-voids were observed in these regions. The transition between regions that failed in a trans- and intergranular fashion is sharp. At 800 and 850 °C the entire fracture surface showed signs of environmental damage, indicating failure in an purely intergranular manner. In contrast, when tested below 600 °C or in an inert atmosphere, environmental damage was absent from the fracture surface and ductile failure occurred after uniform elongation.

Fig. 5(a) shows a secondary electron SEM image of the

intergranular fracture surface at 800 °C. Multiple secondary cracks branch off the primary crack which led to failure. In order to investigate these secondary cracks, sections through the failed test pieces were prepared metallographically. Secondary cracks were consistently found along high angle  $\gamma$ -grain boundaries and the incoherent primary  $\gamma'$ -interfaces. These microstructural features are therefore identified as preferred paths for crack propagation in alloy 720Li. EDX mapping showed that the cracked grain boundaries and the incoherent primary  $\gamma'$ -interfaces are decorated with oxidation products. Fatigue cracks under comparable testing conditions have also been found to initiate and propagate along these features in alloy 720Li [37] and N18 [38]. Therefore, the primary  $\gamma'$ -precipitates play a key role in environmentally assisted-crack propagation in alloy 720Li.

A backscattered electron image showing a representative environmental damage zone at an intergranular crack tip is shown in Fig. 6(a). A local EDX analysis revealed that this damaged zone contains oxides consisting of Ni, Co, Ti, Cr and Al (Fig. 6(b)). The elemental distribution shown in the EDX elemental maps correlate to the contrast seen in the SEM ESB backscattered electron image (a). In order to overcome the problems in EDX analysis posed by the overlap of the O  $K_{\alpha}$  and Cr  $L_{\alpha}$  peaks at 0.525 and 0.573 keV respectively, NanoSIMS analysis of the same area was employed. The selection in the NanoSIMS of the  $^{16}\text{O}^-$ ,  $^{58}\text{Ni}^{16}\text{O}^-$ ,  $^{52}\text{Cr}^{16}\text{O}^-$  and  $^{27}\text{Al}^{16}\text{O}^-$  at masses 16, 74, 68 and 43 amu allowed the distribution of O, Al, Ni and Cr to be studied at this location with a spatial resolution below 100 nm and with the local sensitivity at the ppm level. The NanoSIMS maps in Fig. 6(c) together with the EDX elemental maps show a layered structure of the oxide at and ahead of the crack tip comprising Ni- and Co-, Cr-, Ti- and Al-rich layers. This oxide sequence is in agreement with their relative thermodynamic stability. The oxidation damage zone is observed to penetrate into the primary  $\gamma'$ -precipitates and the  $\gamma$ -grain boundaries. An external Ni- and Co-rich oxide is observed at the beginning of each oxide intrusion. This layer is porous and polycrystalline (Fig. 6(a)). Between this oxide and the  $\gamma$ -grain a thin Cr-rich layer was detected together with Al-rich features. Between the Ni- and Co-rich layer and the primary  $\gamma'$ -precipitates the Cr-rich layer is followed by an Ti- and Al-rich oxide growing into the primary  $\gamma'$ -precipitate. The tip oxide growing into the uncracked grain boundary is Al-rich. Within the spatial resolution and sensitivity





**Fig. 4.** Optical microscopy images showing representative fracture surfaces of specimens failed between 600 and 850 °C. Surface initiated environmental damage can be seen and distinguished from undamaged regions on the fracture surface. The environmental damage on the fracture surface increases with temperature.

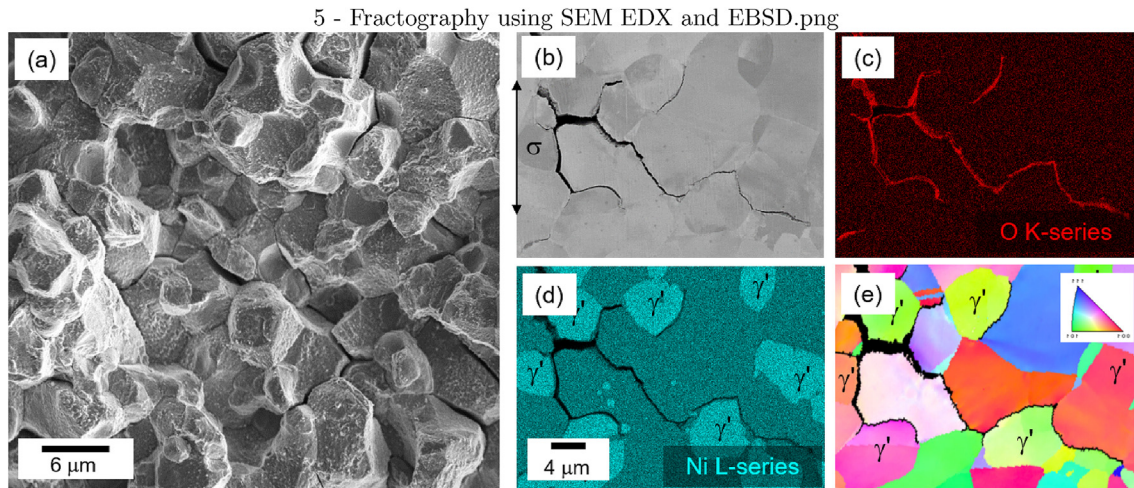


**Fig. 5.** (a) SEM image of an intergranular fracture surface at 800 °C. Grain contours can be clearly identified. (b) Intergranular secondary cracks close to the fracture surface at 800 °C. Cracks which propagated primarily along high angle  $\gamma$ -grain boundaries and incoherent primary  $\gamma'$ -interfaces are filled with oxidation products. These observations were confirmed using EDX mapping (c), (d) and EBSD (e).

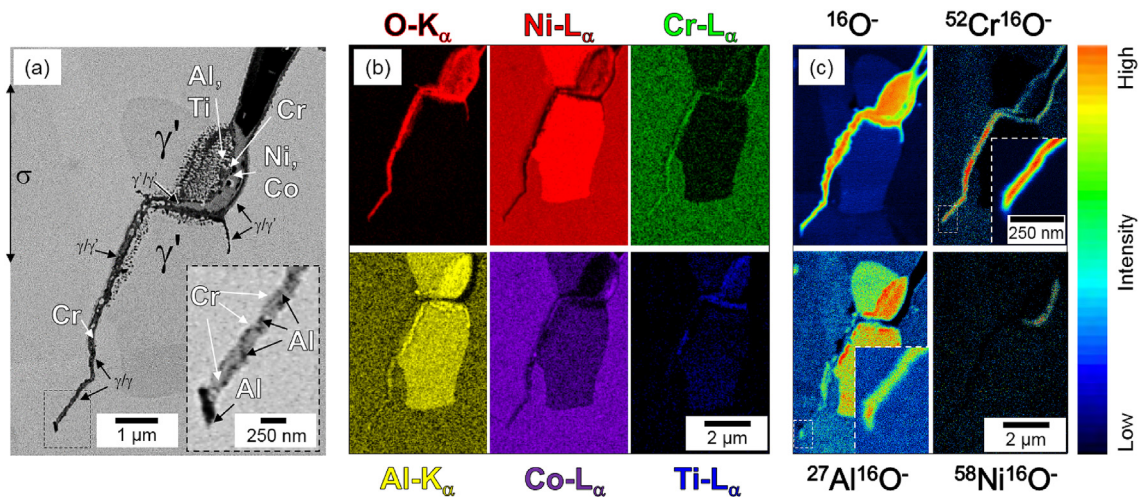


**Fig. 6.** (a) ESB image showing an environmentally-induced damage zone at and ahead of a secondary crack tip along a primary  $\gamma'$ -interface and a  $\gamma$ -grain boundary after slow strain-rate testing at 850 °C. The Z-contrast suggests Al-rich oxide particles within a Cr-rich oxide layer. (b) Corresponding EDX maps showing the formation of Ni-, Co-, Cr-, Ti- and Al-rich oxidation products at and ahead of the crack tip. (c) Corresponding NanoSIMS  $^{16}\text{O}^-$ ,  $^{58}\text{Ni}^{16}\text{O}^-$ ,  $^{52}\text{Cr}^{16}\text{O}^-$  and  $^{27}\text{Al}^{16}\text{O}^-$  maps confirming the simultaneous occurrence of both Cr- and Al-rich oxides at the crack tip.

limits of NanoSIMS elemental oxygen was not observed ahead of the oxide intrusion which is in general agreement with recent studies [6,8,9].

HR-EBSD was used to calculate an estimate of the GND density distribution with a patch size of 50 nm at microstructure specific damage sites at 800 and 950 °C. The technique used to calculate the

GND density is described elsewhere [39]. Slow strain-rate tests were performed at these temperatures and terminated at 4% strain. At 800 °C – in the mid-temperature regime – quasi-brittle failure was observed. At 950 °C – in the high-temperature regime – alloy 720Li did not fail at 4% and the straining was interrupted. Fig. 7(a) and (b) illustrate the damage sites in these tests. While at 800 °C

failure occurs along the  $\gamma$ -grain boundaries and at  $\gamma'$ -precipitates, at 950 °C intragranular ductile voiding and tearing is observed. At these damage sites, GND density distributions were calculated from the lattice curvatures obtained from HR-EBSD measurements, shown in Fig. 7(d) and (f). At 800 °C, distinct grain boundary regions with an increase in GND density can be observed along the cracked and uncracked  $\gamma$ -grain boundaries and primary  $\gamma'$ -precipitates (Fig. 7(d)). At 950 °C dislocations were not observed to accumulate at the grain boundaries. Moreover, the grain boundaries were observed to migrate due to dislocations aligning at 45° to the tensile loading axis. High GND density very low angle boundaries were also seen in this alignment and seemed to suggest some interactions with a  $\gamma$ -grain boundary, see Fig. 7(f).

### 3.4. Measurement of the oxidation kinetics

Thermo-gravimetric analysis was performed on alloy 720Li between 700 and 1000 °C for 50 h and for 10 min in order to quantify the steady-state and pre-steady-state oxidation kinetics. Fig. 8(a) shows the specific mass gains during 50 h exposure. The reaction kinetics were assessed through mass change measurements in the following manner:

$$\left(\frac{m}{A}\right)^2 = k_p'' \cdot t, \quad (4)$$

where  $A$  is the area over which the reaction occurs,  $m$  is the mass,  $k_p''$  is the parabolic oxidation rate constant and  $t$  is time [40]. The oxidation kinetics were seen to increase with temperature and duration in a parabolic manner, see Fig. 8(a). This response replicates the kinetic response of typical chromia forming Ni-based superalloys such as RR1000 [41]. A cross-sections perpendicular to the oxidised surface at 800 °C shows the sequence of oxide layers after 50 h: a dense top layer, presumably  $\text{Cr}_2\text{O}_3$ , and sub-surface internal oxidation zone, presumably  $\text{Al}_2\text{O}_3$ . This is illustrated in Fig. 8(a). The protective chromia surface layer was confirmed by calculating the activation energy for oxide formation using the average parabolic rate constants,  $k_p''$ , shown in Table 5 using the following equation:

$$k_p'' = C_3 \cdot \exp\left(\frac{-Q}{RT}\right), \quad (5)$$

where  $Q$  is the activation energy for oxide formation,  $R$  is the

universal gas constant,  $C_3$  is a constant and  $T$  is the test temperature. A linear fit with an adjusted  $R^2$  of 94.6% was used to calculate the activation energy from the Arrhenius plot resulting in  $Q \approx 325 \text{ kJ mole}^{-1}$ . This indeed confirms the formation of a protective Cr-layer [41].

After 10 min of exposure in laboratory air the formation of a thin surface oxide layer is observed at the metal/gas interface at all test temperatures. Fig. 8(b) illustrates the oxide formed on the surfaces between 700 and 1000 °C. The thickness of these oxide layers were assessed using FIB cross-sections and were found to increase linearly with increasing temperature. An example cross-section at 800 °C is shown in Fig. 8. The relationship between the oxide thickness on top of  $\gamma$ -grains and exposure time at a given temperature can be expressed as:

$$x^2 = 2k_p' \cdot t, \quad (6)$$

where  $k_p'$  is the scaling constant and  $t$  is time [40]. The deduced scaling rate constants  $k_p'$  are given in Table 5. A linear fit with an adjusted  $R^2$  of 98.5% was used to calculate the activation energy from the Arrhenius plot resulting in  $Q \approx 120 \text{ kJ mole}^{-1}$ . This is unambiguously smaller than the activation energy necessary for chromia formation ( $Q \approx 325 \text{ kJ mole}^{-1}$ ). Therefore, a  $(\text{Ni}_{1-x}\text{Co}_x)\text{O}$  is assumed to form on the free surface in the early stages of transient oxidation over the temperature range investigated. Below 900 °C the majority of the oxidation damage was observed to be limited to  $\gamma$ -grain boundaries and the primary  $\gamma'$ -precipitates (Fig. 8(b)). No evidence of environmental damage was observed for special  $\Sigma 3$  grain boundaries. The cross-section shown in Fig. 8(c) shows the enhanced environmental damage at a  $\gamma$ -grain boundary. Porosity and an oxide intrusion can be seen. As exposure temperature is increased the bulk of the  $\gamma$ -grains become equally susceptible to oxidation damage relative to the  $\gamma$ -grain boundaries and primary  $\gamma'$ -precipitates. This is evident at temperatures above 900 °C where the surface of  $\gamma$ -grains showed a comparable amount of environmental damage compared to the grain boundaries and the primary  $\gamma'$ -precipitates. At 1000 °C  $\gamma$ -grain boundaries and the primary  $\gamma'$ -precipitates could not be distinguished on the sample surface.

### 4. Discussion

The results presented above demonstrate conclusively that alloy 720Li is prone to intergranular embrittlement in air at 600–850 °C. But these findings require rationalisation so that the physical

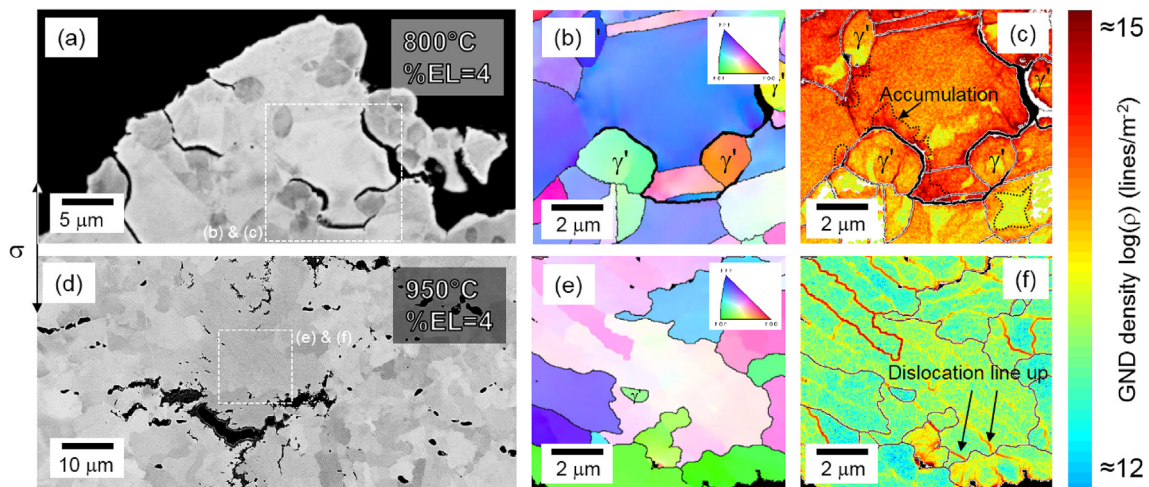


**Fig. 7.** (a) Back-scatter electron image perpendicular to the fracture surface at 800 °C and (d) at 950 °C after 4% strain. (b) and (e) shows EBSD maps at the damage sites. Corresponding maps of GND densities calculated from measured lattice curvatures obtained from EBSD data are shown in (c) and (f), respectively. The overlaid grain boundary positions have a misorientation exceeding 15°.



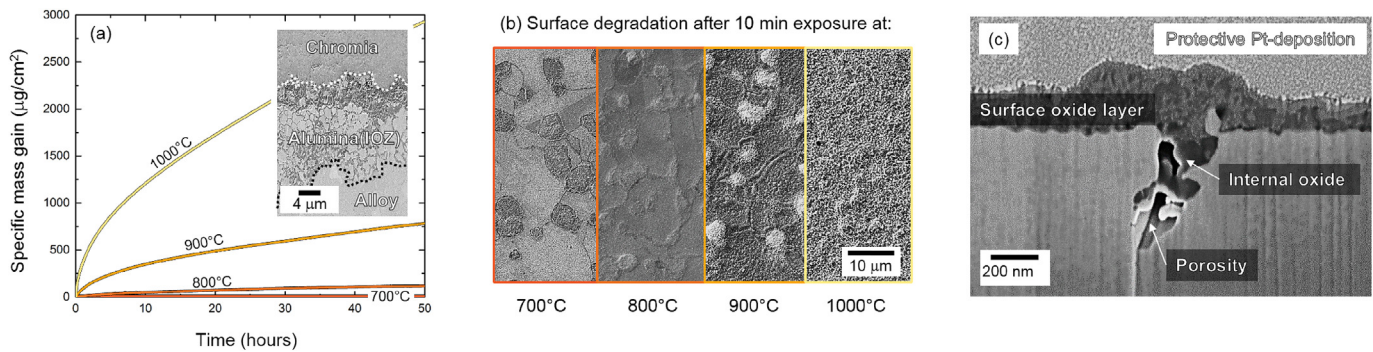


**Fig. 8.** (a) Specific mass gains during 50 h exposure time between 700 and 1000 °C. The typical oxide sequence after 50 h at 800 °C consisting of a chromia and internal alumina is shown. (b) Micrographs of oxygen attack on the sample surface after 10 min between 700 and 1000 °C. The  $\gamma$ -grain boundaries and primary  $\gamma'$ -precipitates oxidise faster than the bulk of the  $\gamma$ -grains. (c) Focused ion beam cross section of  $\gamma$ -grain boundary damage after 10 min of exposure in laboratory air at 800 °C. Beneath the protective Pt-layer an oxide layer and a grain boundary intrusion is visible.

**Table 5**

Average scaling rate constants  $k_p^s$  and parabolic rate constants  $k_p^p$  for alloy 720Li between 600 and 1000 °C.

Temperature (°C)	$k_p^s$ ( $\text{cm}^2 \text{s}^{-1}$ )	$k_p^p$ ( $\text{mg}^2 \text{cm}^{-4} \text{s}^{-1}$ )
700	$8.3 \cdot 10^{-14}$	$2.2 \cdot 10^{-9}$
800	$5.2 \cdot 10^{-13}$	$8.2 \cdot 10^{-8}$
900	$1.3 \cdot 10^{-12}$	$5.4 \cdot 10^{-7}$
1000	—	$4.7 \cdot 10^{-5}$

mechanisms and chemical reactions causing this effect can be better understood. Moreover, the ramifications particularly for the optimisation of heat treatment of high strength superalloys need to be elucidated.

#### 4.1. On the mechanism of intergranular oxidation

Of critical importance is the observation of an internal oxidation zone which has been shown to penetrate the  $\gamma$ -grain boundaries and primary  $\gamma'$ -interfaces. By making use of bend testing of microcantilevers, this environmental damage zone has been shown to be brittle [14]; this explains the decrease of tensile ductility above 500 °C. It is also consistent with the reported increase in dwell fatigue crack propagation rate above 500 °C which has been reported for many alloys including 720Li [42]. Also relevant is the acceleration in oxidation kinetics with increasing temperature; this rationalises the decrease in ductility with temperature up to 750 °C. Nonetheless, it is the precise details of the internal oxidation process which are of prime concern; as different oxidation reactions are occurring and it is to be expected that not all of these are equally damaging.

Consider the oxidation reactions which might be expected to occur – on the basis of established oxidation behaviour of nickel-based superalloys on plane, polished surfaces – at a notch being subjected to an oxidative environment, see Fig. 9. In the first instance we imagine that the crack is progressing along a  $\gamma$  grain boundary. It is well established that NiO and CoO oxides are likely to form quickly in an outward fashion, at a rate controlled by the migration of  $\text{Ni}^{2+}$  and  $\text{Co}^{2+}$  ions through the oxide [43]. On this basis,  $(\text{Ni}_{1-x}\text{Co}_x)\text{O}$  is expected to fill the cracked notch rather than extending it, but with porosity remaining in the substrate below it which is consistent with the evidence of Fig. 8(c). Consistent with the very lowest equilibrium partial pressures of oxygen,  $\text{Al}_2\text{O}_3$  is expected to arise with the deepest penetration, growing inwards at a rate controlled by  $\text{O}^{2-}$  migration inwards. A region of  $\text{Cr}_2\text{O}_3$  is expected above the  $\text{Al}_2\text{O}_3$ . A three layer oxide structure has been proposed in the literature to occur at the crack tip [6], see Fig. 9(a).

There is also the possibility of a spinel layer  $\text{NiCr}_2\text{O}_4$  existing between NiO and  $\text{Cr}_2\text{O}_3$ . In addition,  $\text{TiO}_2$  can precipitate alongside of  $\text{Cr}_2\text{O}_3$  and  $\text{Al}_2\text{O}_3$ . In contrast to oxidation on plane polished surfaces mass transport of ion species by volume diffusion is not required at a crack tip. Note that – unlike the case of oxidation on a plane, polished surface – matrix/oxide interfaces are aligned parallel to the direction of oxide growth and are thus available as short-circuit diffusion paths resulting in the oxide growth into the grain boundary.

What is found in practice at a crack tip in this study is broadly consistent with the above simplified picture but differs from it in some important respects. For instance, the order of the reaction products is consistent with an Al-rich oxide (presumably  $\text{Al}_2\text{O}_3$ ) at the furthest extent and Ni- and Co-rich oxides –  $(\text{Ni}_{1-x}\text{Co}_x)\text{O}$  and/or spinel – closer to the crack tip, with Cr-rich oxides ( $\text{Cr}_2\text{O}_3$ ) lying in-between. The elemental maps in Fig. 6(b) suggest the internal formation of an Ti-rich oxide (presumably  $\text{TiO}_2$ ) particles alongside of the alumina. This is consistent with [44]. Additionally, the

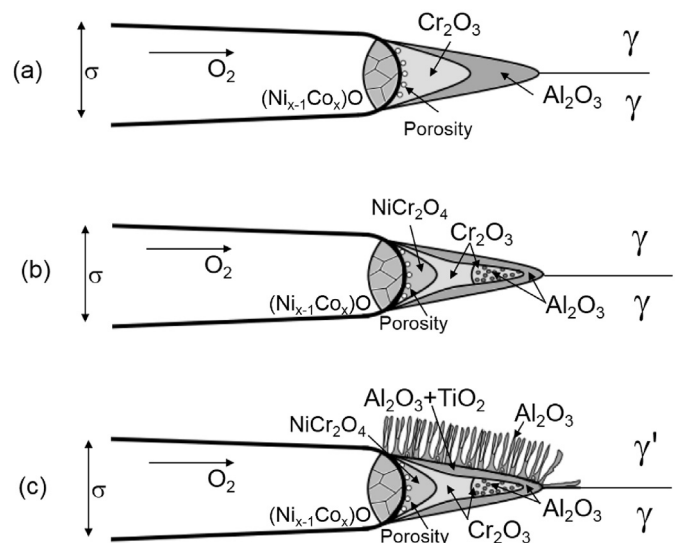


**Fig. 9.** (a) Schematic diagram of the oxidation morphology of a layered crack tip oxide in the thermodynamic sequence of NiO,  $\text{Cr}_2\text{O}_3$  and  $\text{Al}_2\text{O}_3$ . (b) and (c) Schematic diagram of the oxidation morphology observed in alloy 720Li at a  $\gamma$ -grain boundary and at a primary  $\gamma'$ -interface. An external NiO layer is formed at the intergranular crack with an inner layer  $\text{NiCr}_2\text{O}_4$ . Oxygen diffusion results in the formation of  $\text{Cr}_2\text{O}_3$  subscale,  $\text{Al}_2\text{O}_3$  is dissolved within this subscale before a continuous  $\text{Al}_2\text{O}_3$  layer is formed. The primary  $\gamma'$ -interface shows internal  $\text{Al}_2\text{O}_3$  formation.



contentious damage zone extension during the process of crack propagation requires that alumina dissolves within the chromia at the  $\gamma$ -grain boundary, and evidence exists that this is indeed occurring, see Fig. 6. Here, it was shown that the  $\gamma$ -grain boundary ahead of the crack tip consists of what seems to be Al-rich oxides embedded in a Cr-rich oxide. These observations are based on the elemental contrast of the energy selective backscatter (ESB) detector. This is illustrated for steady-state crack extension in Fig. 9(b). But importantly, the  $\gamma$ -grain boundaries and the primary  $\gamma'$ -interfaces are found to oxidise at markedly different rates, see Fig. 9(c). This finding has some important implications for the optimisation of the heat treatment of polycrystalline superalloys for resisting oxidation-assisted cracking, as discussed further in Section 4.3.

#### 4.2. On the role of grain boundary sliding and grain boundary mobility

Intergranular oxidation attack explains the decrease in ductility between 500 and 750 °C due to the increase in oxidation kinetics with increasing temperature. However, this fails to explain the increase in ductility above 750 °C. Here we postulate that in the mid-temperature regime slip-assisted grain boundary sliding plays a role in the quasi-brittle failure of the environmentally-damaged grain boundaries. This idea is consistent with those of [18]. As the temperature rises, ductility recovers due to an increase in grain boundary mobility. Moreover, grain boundary sliding is active in the mid-temperature regime and its occurrence is accommodated by the formation of dislocation cell structures in the vicinity of the grain boundaries. Those act as obstacles in the slip plane leading to stress build up at the damaged  $\gamma$ -grain boundaries and  $\gamma'$ -interfaces. The resulting stress concentrations lead to quasi-brittle failure of the intergranular oxides at and ahead of the crack tip.

That slip-assisted grain boundary sliding is arising in the mid-temperature regime is supported if the activation energy, the strain-rate sensitivity and the activation volume are estimated. The activation energy  $Q$  for the deformation process providing the temperature dependence of the flow stress between 700 and 850 °C can be estimated as  $Q \approx 40 \text{ kJ mol}^{-1}$ , see Equation (1). This is lower than the activation energy necessary for nickel-self diffusion ( $\approx 300 \text{ kJ mol}^{-1}$  [45]) in the  $\gamma$ -matrix or the activation energy necessary to unpin Kear-Wilsdorf locks ( $\approx 300\text{--}600 \text{ kJ mol}^{-1}$  [46]). The deduced activation energy is closer to values reported for grain boundary self-diffusion in nickel ( $\approx 20\text{--}70 \text{ kJ mol}^{-1}$  [45,47]). This suggests a thermally-activated deformation process involving diffusion along the grain boundaries. The authors suggest that grain boundary self diffusion is linked to accommodating grain boundary sliding in the studied temperature and strain-rate regime. Grain boundary sliding at the applied test conditions has to be assisted by plastic deformation in the near grain boundary regions. Thus, the grain boundary sliding-rate is governed by an independent process which can be assessed through the strain-rate sensitivity,  $m$ , and through the activation volume,  $\Delta V$ . Equations (2) and (3) lead to  $m \approx 0.17$  and  $\Delta V \approx 65 b^3$ . For rate-dependent deformation process of the Coble-creep type the strain-rate dependence would be expected to be higher ( $m \approx 1$  [48]) and the activation volume would be of order the atomic spacing ( $\Delta V \approx 1 b^3$  [49]). The strain-rate sensitivity parameter of  $m \approx 0.17$  suggests the grain boundary sliding rate to be dependent on either climb-controlled or cross-slip controlled dislocation creep mechanisms. During climb-controlled dislocation creep obstacles are overcome by means of vacancy diffusion ( $\Delta V \approx 1 b^3$ ). In order to cross-slip, screw-dislocations have to dissociate forming a stacking fault typically of the order of  $10\text{--}100 b^3$  [36]. This is the same order of magnitude as the activation volume observed here ( $\Delta V \approx 65 b^3$ ). Cross-slip is supported

by previous TEM observations where tangles of dislocations were observed in addition to the presence of stacking faults within secondary  $\gamma'$ -particles during homogeneous tensile deformation at 750 °C and  $1 \cdot 10^{-5} \text{ s}^{-1}$  [24]. Creep through grain boundary sliding has been observed in ME3 under dwell loading conditions at 704 and 760 °C [50]. This was also suggested for NR3 at 700 °C during creep deformation [51]. The grain boundary sliding rate can therefore be associated with the movement of dislocations through a region with a very high dislocation density or the emission of mobile dislocations from the grain boundaries into this affected grain boundary region.

The role of slip-assisted grain boundary sliding in the mid-temperature regime is confirmed when HR-EBSD is applied. Fig. 7 (d) shows distinct regions with an increase in GND density along the  $\gamma$ -grain boundaries and primary  $\gamma'$ -precipitates at 800 °C after 4% strain. This suggests a low grain boundary mobility and it seems probable that the inhibition of sliding and migration of grain boundaries in the mid-temperature regime leads to dislocation tangles and pileups which produce local stress concentrations as explained above. In contrast, at 950 °C the ability to relieve local stresses at the damaged grain boundary increases significantly leading to the observed recovery in tensile ductility. This thermally activated mobility is likely to be linked to the onset of  $\gamma'$ -precipitate dissolution. In addition, the absence of enhanced oxidation damage during short term exposure suggests that grain boundary diffusion starts to become less favourable relative to lattice diffusion, see Fig. 8. Therefore, oxide growth into the grain boundary is less pronounced in the high temperature regime.

To summarise, the behaviour of the grain boundaries explains the increase in ductility above 750 °C. It is the increase in grain boundary mobility with temperature – locally or during dynamic recrystallisation – which is the key effect. The observed three temperature regimes with regards to the tensile ductility are illustrated in Fig. 10.

#### 4.3. On the influence of heat treatment on embrittlement

This work confirms that sub-solvus alloys such as 720Li are susceptible to environmentally-assisted cracking at operation-relevant temperatures. The microstructure conferred by the sub-solvus heat treatment exacerbates oxidation-assisted cracking mainly due to two reasons. First, the primary  $\gamma'$ -precipitates,  $\text{Ni}_3(\text{Al,Ti})$ , act as nucleation sites for external  $\text{NiO}$  and internal  $\text{TiO}_2$  and  $\text{Al}_2\text{O}_3$  formation, see Fig. 9(c). Second, the relatively small  $\gamma$ -grain size of the alloy promotes the onset of slip-assisted grain boundary sliding and the accumulation of dislocations at the grain boundaries in the mid-temperature regime.

Consequently, a super-solvus heat treatment will modify the microstructure, dissolving primary  $\gamma'$ -precipitates and allowing  $\gamma$ -grain growth. The identified relationship of tensile ductility to microstructure indicates that such changes will lead to an improvement in tensile ductility in the mid-temperature regime, prohibiting the onset of intergranular oxidation-assisted cracking. However, the resulting loss in alloy strength due to the increase in  $\gamma$ -grain size and the absence of primary  $\gamma'$ -precipitates can be counteracted by means of composition [52]. Creep properties will be improved due to the increase in  $\gamma$ -grain size. This is confirmed when alloy RR1000 was tested in both sub- and super-solvus heat treated condition in the mid-temperature regime. The increase in tensile ductility after a super-solvus heat treatment can be rationalised in the following way. First, the super-solvus heat treatment increases the  $\gamma$ -grain size. Therefore, slip-assisted grain-boundary sliding is not dominating in the studied temperature regime. Second, primary  $\gamma'$ -precipitates are dissolved. Both changes lower the magnitude of stress build up at the  $\gamma$ -grain boundaries and delays

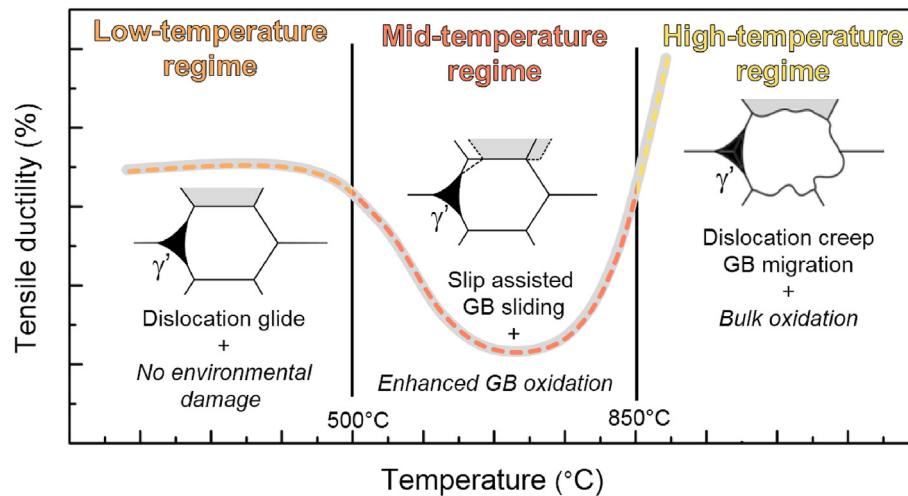


**Fig. 10.** Schematic illustration of the interplay between environmental damage and apparent deformation mechanism responsible for the observed temperature dependent ductility in Alloy 720Li.

the accumulation of dislocations at the grain boundaries. In addition, the overall grain boundary content is reduced. This explains why the details of the heat treatment used for polycrystalline superalloys – and the associated changes in microstructure – influence the time-dependent crack growth behaviour of turbine disc alloys regardless of the chemical composition as demonstrated by Ref. [12]. A correlation between the macroscopic tensile strength and ductility is not observed, see Table 4.

## 5. Summary and conclusions

The following specific conclusions can be drawn from this work:

- (1) The temperature dependence of the tensile ductility is characterised by three distinct regimes. Below 600 °C, the oxidising environment does not affect the ductility which then exceeds 15%; failure is transgranular as a result of homogeneous dislocation slip. But between 600 and 850 °C, ductility is reduced substantially with a pronounced minimum found at 750 °C of a few percent; intergranular quasi-brittle failure is then observed. Above 850 °C, tensile ductility is recovered and it exceeds 25%.
- (2) In the embrittled regime, the oxidation damage occurs preferentially at incoherent primary  $\gamma'$ -precipitates and at high angle  $\gamma$ -grain boundaries. Growth of internal oxide intrusions at these interfaces is the cause of the limited tensile ductility and the quasi-brittle failure. The oxide intrusions contain different phases present in an order consistent with thermodynamics and the expected gradient in equilibrium partial pressure of oxygen. Thus  $(\text{Ni}_{(1-x)}\text{Co}_x)\text{O}$  is followed by spinel and closer to the crack tip  $\text{Cr}_2\text{O}_3$ ,  $\text{TiO}_2$  and finally  $\text{Al}_2\text{O}_3$ . Evidence is shown indicating alumina dissolution within the chromia layer during steady-state crack propagation. The amount of oxidation damage increases with temperature and time, thus explaining the rather more ductile behaviour at high deformation rates.
- (3) The mechanism of embrittlement involves slip-assisted grain boundary sliding which causes the accumulation of dislocations in the vicinity of the grain boundaries. The resulting local stresses fracture the crack-tip oxides, causing intergranular crack propagation. As the temperature is increased, grain boundaries migrate thus delaying stress build up. This explains the regained ductility above 750 °C. Above 900 °C

grain boundaries are fully mobile and intergranular fracture does not occur.

- (4) This work has implications for the choice of heat treatment temperature for polycrystalline nickel-based superalloys. A sub-solvus heat treatment exacerbates oxidation-assisted cracking. First, the concomitant – relatively small – grain size promotes the build-up of dislocations at the grain boundaries. Second, the primary  $\gamma'$ -precipitates act as nucleation sites for oxide formation, in particular Ni, Ti, and Al-rich ones. Conversely, a super-solvus heat treatment dissolves primary  $\gamma'$ -precipitates and increases the  $\gamma$ -grain size in a favourable fashion, thus reducing the susceptibility to oxidation-assisted cracking.
- (5) It seems likely that our results explain why the details of the heat treatment used for polycrystalline superalloys – for example above or below the solvus temperature – influence the performance of these alloys under so-called dwell fatigue crack propagation conditions.

## Acknowledgments

The financial support of this work via the Engineering and Physical Sciences Research Council (EPSRC) (EP/M50659X/1) and Rolls-Royce plc. is acknowledged by André Németh. David Armstrong acknowledges financial support from the Royal Academy of Engineering through a Research Fellowship.

## References

- [1] R. Jiang, P.A.S. Reed, Critical Assessment 21: oxygen-assisted fatigue crack propagation in turbine disc superalloys, *Mater. Sci. Technol.* 32 (5) (2016) 401–406, <http://dx.doi.org/10.1080/02670836.2016.1148227>.
- [2] U. Krupp, W. Kane, C. Laird, C. McMahon, Brittle intergranular fracture of a Ni-base superalloy at high temperatures by dynamic embrittlement, *Mater. Sci. Eng. A* 387–389 (2004) 409–413, <http://dx.doi.org/10.1016/j.msea.2004.05.053>.
- [3] W.M. Kane, C. McMahon, Part II. Effects of grain-boundary structure on the path of cracking in polycrystals, *Mater. Sci. Eng. A* 507 (1–2) (2009) 61–65, <http://dx.doi.org/10.1016/j.msea.2008.07.015>.
- [4] H.-J. Christ, K. Wackermann, U. Krupp, Effect of dynamic embrittlement on high temperature fatigue crack propagation in IN718 experimental characterisation and mechanism-based modelling, *Mater. High. Temp.* 33 (4–5) (2016) 528–535, <http://dx.doi.org/10.1080/09603409.2016.1187464>.
- [5] J. Pfandtner, C. McMahon Jr., Oxygen-induced intergranular cracking of a Ni-base alloy at elevated temperatures an example of dynamic embrittlement, *Acta Mater* 49 (16) (2001) 3369–3377, [http://dx.doi.org/10.1016/S1359-6454\(01\)00005-2](http://dx.doi.org/10.1016/S1359-6454(01)00005-2).

- [6] H. Kitaguchi, H. Li, H. Evans, R. Ding, I. Jones, G. Baxter, P. Bowen, Oxidation ahead of a crack tip in an advanced Ni-based superalloy, *Acta Mater.* 61 (6) (2013) 1968–1981, <http://dx.doi.org/10.1016/j.actamat.2012.12.017>.
- [7] H. Evans, H. Li, P. Bowen, A mechanism for stress-aided grain boundary oxidation ahead of cracks, *Scr. Mater.* 69 (2) (2013) 179–182, <http://dx.doi.org/10.1016/j.scriptamat.2013.03.026>.
- [8] L. Viskari, M. Hörnqvist, K. Moore, Y. Cao, K. Stiller, Intergranular crack tip oxidation in a Ni-base superalloy, *Acta Mater.* 61 (10) (2013) 3630–3639, <http://dx.doi.org/10.1016/j.actamat.2013.02.050>.
- [9] H. Li, J. Sun, M. Hardy, H. Evans, S. Williams, T. Doel, P. Bowen, Effects of microstructure on high temperature dwell fatigue crack growth in a coarse grain PM nickel based superalloy, *Acta Mater.* 90 (2015) 355–369, <http://dx.doi.org/10.1016/j.actamat.2015.02.023>.
- [10] M. Hörnqvist, L. Viskari, K.L. Moore, K. Stiller, High-temperature crack growth in a Ni-base superalloy during sustained load, *Mater. Sci. Eng. A* 609 (2014) 131–140, <http://dx.doi.org/10.1016/j.msea.2014.04.102>.
- [11] H. Kitaguchi, M. Moody, H. Li, H. Evans, M. Hardy, S. Lozano-Perez, An atom probe tomography study of the oxide/metal interface of an oxide intrusion ahead of a crack in a polycrystalline Ni-based superalloy, *Scr. Mater.* 97 (2015) 41–44, <http://dx.doi.org/10.1016/j.scriptamat.2014.10.025>.
- [12] J. Telesman, P. Kantzos, J. Gayda, P. Bonacuse, A. Prescenzi, Microstructural variables controlling time-dependent crack growth in a P/M superalloy, in: *Superalloys 2004* (Tenth Int. Symp., TMS, 2004, pp. 215–224, [http://dx.doi.org/10.7449/2004/Superalloys\\_2004\\_215\\_224](http://dx.doi.org/10.7449/2004/Superalloys_2004_215_224).
- [13] T.P. Gabb, J. Telesman, A. Banik, E. McDevitt, Use of slow strain rate tensile testing to assess the ability of several superalloys to resist environmentally-assisted intergranular cracking, in: 8th Int. Symp. Superalloy 718 Deriv, John Wiley & Sons, Inc, Hoboken, NJ, USA, 2014, pp. 697–712, <http://dx.doi.org/10.1002/9781119016854.ch54>.
- [14] A.A.N. Németh, D.J. Crudden, D.M. Collins, D.E.J. Armstrong, R.C. Reed, Novel techniques to assess environmentally-assisted cracking in a nickel-based superalloy, in: *Superalloys 2016*, John Wiley & Sons, Inc, Hoboken, NJ, USA, 2016, pp. 801–810, <http://dx.doi.org/10.1002/9781119075646.ch86>.
- [15] A.K. Roy, A. Venkatesh, V. Marthandam, A. Ghosh, Tensile deformation of a nickel-base alloy at elevated temperatures, *J. Mater. Eng. Perform.* 17 (4) (2008) 607–611, <http://dx.doi.org/10.1007/s11665-007-9189-x>.
- [16] M. Rezendé, L. Araújo, S. Gabriel, J. Dille, L. de Almeida, Oxidation assisted intergranular cracking under loading at dynamic strain aging temperatures in Inconel 718 superalloy, *J. Alloys Compd.* 643 (2015) S256–S259, <http://dx.doi.org/10.1016/j.jallcom.2014.12.279>.
- [17] D.A. Woodford, H.D. Solomon, L.F. Coffin, Mechanical behavior of materials, in: *2nd International Conf. Mech. Behav. Mater.*, 1976, 983–987.
- [18] D.A. Woodford, Gas phase embrittlement and time dependent cracking of nickel based superalloys, *Energy Mater* 1 (1) (2006) 59–79, <http://dx.doi.org/10.1179/174892306X99679>.
- [19] J. Telesman, T. Gabb, A. Garg, P. Bonacuse, J. Gayda, Effect of microstructure on time dependent fatigue crack growth behavior in a P/M turbine disk alloy, in: *Superalloys 2008* (Eleventh Int. Symp., TMS, 2008, pp. 807–816, [http://dx.doi.org/10.7449/2008/Superalloys\\_2008\\_807\\_816](http://dx.doi.org/10.7449/2008/Superalloys_2008_807_816).
- [20] J. Telesman, T. Gabb, L. Ghosn, Separating the influence of environment from stress relaxation effects on dwell fatigue crack growth in a nickel-base disk alloy, in: *Superalloys 2016*, John Wiley & Sons, Inc, Hoboken, NJ, USA, 2016, pp. 549–560, <http://dx.doi.org/10.1002/9781119075646.ch59>.
- [21] D. Furrer, H.-J. Fecht, Microstructure and mechanical property development in superalloy U720LI, in: *Superalloys 2000* (Ninth Int. Symp., TMS, 2000, pp. 415–424, [http://dx.doi.org/10.7449/2000/Superalloys\\_2000\\_415\\_424](http://dx.doi.org/10.7449/2000/Superalloys_2000_415_424).
- [22] G. Osinkolu, G. Onofrio, M. Marchionni, Fatigue crack growth in polycrystalline IN 718 superalloy, *Mater. Sci. Eng. A* 356 (1–2) (2003) 425–433, [http://dx.doi.org/10.1016/S0921-5093\(03\)00156-4](http://dx.doi.org/10.1016/S0921-5093(03)00156-4).
- [23] S. Chiozzi, V. Dattoma, R. Nobile, Mechanical behaviour of udimet 720Li superalloy, in: *Exp. Anal. Nano Eng. Mater. Struct.*, Springer Netherlands, Dordrecht, 2007, pp. 463–464, [http://dx.doi.org/10.1007/978-1-4020-6239-1\\_230](http://dx.doi.org/10.1007/978-1-4020-6239-1_230).
- [24] K. Gopinath, A. Gogia, S. Kamat, R. Balamuralikrishnan, U. Ramamurty, Tensile properties of Ni-Based superalloy 720Li: temperature and strain rate effects, *Metall. Mater. Trans. A* 39 (10) (2008) 2340–2350, <http://dx.doi.org/10.1007/s11661-008-9585-3>.
- [25] K. Gopinath, A. Gogia, S. Kamat, U. Ramamurty, Dynamic strain ageing in Ni-base superalloy 720Li, *Acta Mater.* 57 (4) (2009) 1243–1253, <http://dx.doi.org/10.1016/j.actamat.2008.11.005>.
- [26] N. Iqbal, J. Rolph, R. Moat, D. Hughes, M. Hofmann, J. Kelleher, G. Baxter, P.J. Withers, M. Preuss, A comparison of residual stress development in inertia friction welded fine grain and coarse grain nickel-base superalloy, *Metall. Mater. Trans. A* 42 (13) (2011) 4056–4063, <http://dx.doi.org/10.1007/s11661-011-0802-0>.
- [27] D.M. Knowles, D.W. Hunt, The influence of microstructure and environment on the crack growth behavior of powder metallurgy nickel superalloy RR1000, *Metall. Mater. Trans. A* 33 (10) (2002) 3165–3172, <http://dx.doi.org/10.1007/s11661-002-0302-3>.
- [28] C. Stöcker, M. Zimmermann, H.-J. Christ, Z.-L. Zhan, C. Cornet, L. Zhao, M. Hardy, J. Tong, Microstructural characterisation and constitutive behaviour of alloy RR1000 under fatigue and creep/fatigue loading conditions, *Mater. Sci. Eng. A* 518 (1–2) (2009) 27–34, <http://dx.doi.org/10.1016/j.msea.2009.04.055>.
- [29] B. Roebuck, D. Cox, R. Reed, An innovative device for the mechanical testing of miniature specimens of superalloys, in: *Superalloys 2004* (Tenth Int. Symp., TMS, 2004, pp. 523–528, [http://dx.doi.org/10.7449/2004/Superalloys\\_2004\\_523\\_528](http://dx.doi.org/10.7449/2004/Superalloys_2004_523_528).
- [30] A.J. Wilkinson, G. Meaden, D.J. Dingley, High-resolution elastic strain measurement from electron backscatter diffraction patterns: new levels of sensitivity, *Ultramicroscopy* 106 (4–5) (2006) 307–313, <http://dx.doi.org/10.1016/j.ultramicro.2005.10.001>.
- [31] K.L. Moore, M. Schröder, C.R.M. Grovenor, Imaging secondary ion mass spectroscopy, in: *Handb. Nanoscopy*, Wiley-VCH Verlag GmbH & Co. KGaA, Weinheim, Germany, 2012, pp. 709–744, <http://dx.doi.org/10.1002/9783527641864.ch21>.
- [32] M. Calmunger, G. Chai, S. Johansson, J. Moverare, Deformation behaviour in advanced heat resistant materials during slow strain rate testing at elevated temperature, *Theor. Appl. Mech. Lett.* 4 (4) (2014) 041004, <http://dx.doi.org/10.1063/2.1404104>.
- [33] S. Everitt, M. Starink, P. Reed, Temperature and dwell dependence of fatigue crack propagation in various heat treated turbine disc alloys, in: *Superalloys 2008* (Eleventh Int. Symp., TMS, 2008, pp. 741–750, [http://dx.doi.org/10.7449/2008/Superalloys\\_2008\\_741\\_750](http://dx.doi.org/10.7449/2008/Superalloys_2008_741_750).
- [34] G.E. Dieter, *Mechanical Metallurgy*, McGraw-Hill, New York, 1961, <http://dx.doi.org/10.5962/bhl.title.35895>.
- [35] C. Zener, J.H. Hollomon, Effect of strain rate upon plastic flow of steel, *J. Appl. Phys.* 15 (1) (1944) 22, <http://dx.doi.org/10.1063/1.1707363>.
- [36] D. Caillard, J.L. Martin, *Thermally Activated Mechanisms in Crystal Plasticity*, Pergamon, Amsterdam, 1989.
- [37] H.T. Pang, P.A.S. Reed, Microstructure effects on high temperature fatigue crack initiation and short crack growth in turbine disc nickel-base superalloy Udimet 720Li, *Mater. Sci. Eng. A* 448 (1–2) (2007) 67–79, <http://dx.doi.org/10.1016/j.msea.2006.11.016>.
- [38] R. Jiang, S. Everitt, N. Gao, K. Soady, J. Brooks, P. Reed, Influence of oxidation on fatigue crack initiation and propagation in turbine disc alloy N18, *Int. J. Fatigue* 75 (2015) 89–99, <http://dx.doi.org/10.1016/j.ijfatigue.2015.02.007>.
- [39] P. Littlewood, T. Britton, A. Wilkinson, Geometrically necessary dislocation density distributions in Ti6Al4V deformed in tension, *Acta Mater.* 59 (16) (2011) 6489–6500, <http://dx.doi.org/10.1016/j.actamat.2011.07.016>.
- [40] N. Briks, G.H. Meier, F.S. Pettit, *High-temperature Oxidation of Metals*, Cambridge University Press, Cambridge, 2006, <http://dx.doi.org/10.1007/s13398-014-0173-7.2>.
- [41] M. Taylor, H. Evans, S. Stekovic, M. Hardy, The oxidation characteristics of the nickel-based superalloy, RR1000, at temperatures of 700–900°C, *Mater. High. Temp.* 29 (2) (2012) 145–150, <http://dx.doi.org/10.3184/096034012X13341417107382>.
- [42] H. Li, J. Fisk, L.-B. Lim, S. Williams, P. Bowen, Thresholds of time dependent intergranular crack growth in a nickel disc alloy Alloy 720Li, *MATEC Web Conf.* 14 (2014) 10001, <http://dx.doi.org/10.1051/mateconf/20141410001>.
- [43] R.C. Reed, *The Superalloys*, Cambridge University Press, Cambridge, 2006, <http://dx.doi.org/10.1017/CBO9780511541285>.
- [44] F. Abe, H. Araki, H. Yoshida, M. Okada, The role of aluminum and titanium on the oxidation process of a nickel-base superalloy in steam at 800°C, *Oxid. Met.* 27 (1–2) (1987) 21–36, <http://dx.doi.org/10.1007/BF00656727>.
- [45] A.R. Wazzan, Lattice and grain boundary self-diffusion in nickel, *J. Appl. Phys.* 36 (11) (1965) 3596–3599, <http://dx.doi.org/10.1063/1.1700021>.
- [46] V. Vitek, Y. Sodani, A theory of the temperature and strain rate dependence of the yield stress of L12 compounds in the anomalous regime, *Scr. Metall. Mater.* 25 (4) (1991) 939–944, [http://dx.doi.org/10.1016/0956-716X\(91\)90253-W](http://dx.doi.org/10.1016/0956-716X(91)90253-W).
- [47] W.R. Upthegrove, M. Sinnott, Grain boundary self-diffusion of nickel, *Trans. ASM* 50 (1958) 1031–1046.
- [48] Y. Wang, A. Hamza, E. Ma, Temperature-dependent strain rate sensitivity and activation volume of nanocrystalline Ni, *Acta Mater.* 54 (10) (2006) 2715–2726, <http://dx.doi.org/10.1016/j.actamat.2006.02.013>.
- [49] H. Conrad, Grain size dependence of the plastic deformation kinetics in Cu, *Mater. Sci. Eng. A* 341 (1–2) (2003) 216–228, [http://dx.doi.org/10.1016/S0921-5093\(02\)00238-1](http://dx.doi.org/10.1016/S0921-5093(02)00238-1).
- [50] K. Maciejewski, J. Dahal, Y. Sun, H. Ghonem, Creep/Environment interactions in dwell-fatigue crack growth of nickel based superalloys, *Metall. Mater. Trans. A* 45 (5) (2014) 2508–2521, <http://dx.doi.org/10.1007/s11661-014-2199-z>.
- [51] D. Locq, P. Caron, S. Raujol, F. Pettinari-Sturm, A. Coujou, N. Clement, On the role of tertiary  $\gamma$  precipitates in the creep behaviour at 700°C of a PM disk superalloy, in: *Superalloys 2004* (Tenth Int. Symp., TMS, 2004, pp. 179–187, [http://dx.doi.org/10.7449/2004/Superalloys\\_2004\\_179\\_187](http://dx.doi.org/10.7449/2004/Superalloys_2004_179_187).
- [52] E. Galindo-Nava, L. Connor, C. Rae, On the prediction of the yield stress of unimodal and multimodal  $\gamma$  Nickel-base superalloys, *Acta Mater.* 98 (2015) 377–390, <http://dx.doi.org/10.1016/j.actamat.2015.07.048>.